

Role of Zirconium Conversion Coating in Corrosion Performance of Aluminum Alloys: An Integrated First-Principles and Multiphysics Modeling Approach

Arash Samaei ^a, Santanu Chaudhuri ^{a, b*}

^a Civil, Materials, and Environmental Engineering Department, University of Illinois at Chicago, IL, 60607, United States

^b Argonne National Laboratory, Lemont, IL, 60439, United States

* Corresponding author's email address: santc@uic.edu

Abstract

A variety of chromate-free conversion coatings are being actively investigated to improve the corrosion performance of light-weight alloys for aerospace and defense applications. Advancing conversion coating, however, requires an in-depth understanding of the underlying corrosion mechanisms in order to rationally design sustainable coatings. Here, we present a multiscale modeling approach to predict corrosion performance of metallic materials, with a focus on localized corrosion of Cu-containing aluminum alloys coated with ZrO₂ layer. First-principles and transition-state theory are used to implement the kinetics model, which includes electrolyte-metal interfacial reactions. The modeling framework systematically characterizes and couples multiple electrochemical and physical (e.g., transport) phenomena to explore interrelationships between pit morphology, surface chemistry, and local environment. This multiscale model can quantitatively link the corrosion rate of ZrO₂-coated aluminum alloys with the evolution of interfacial reactions during immersion, which is very difficult to establish using *in situ* experiments. We have evaluated the presented multiscale model using available experimental data. The rate of corrosion and pit stability were quantitatively assessed for various environmental parameters and applied potentials. Results show that Zr-based conversion coating strongly enhances the corrosion performance of aluminum alloys due to zirconium involvement in interfacial kinetics.

Keywords: Multiscale Simulation; Density Functional Theory; Transition State Theory; Finite Element Method; Multiphysics; Corrosion Conversion; Aluminum Alloys; Zirconia; Localized Pitting Corrosion

Nomenclature

Ω_{Al}	Aluminum matrix (anode) domain	φ	Electrostatic potential
Ω_{θ}	θ -phase (cathode) domain	\vec{v}	Flow velocity
Ω_p	Passive oxide layer domain	N^r	Total number of reactions
Ω_e	Electrolyte domain	ω_l^m	Stoichiometric coefficient of species l in the m th reaction
$\partial\Omega_{e-m}$	Solid-liquid interface	k_f^m	Forward reaction rate constant
$E_{Elec(0K)}$	Electronic energy at 0 K	k_b^m	Backward reaction rate constant
E_{298}	Total energy	i_a	Total anodic current density
G_{298}	Gibbs free energy	$i_{a,1}$	Active dissolution current density

H_{298}	Enthalpy	$i_{a,2}$	Oxide formation current density
$\Delta G_{298,act}$	Activation Gibbs free energy at 298 K	θ_0	Oxide coverage fraction
$\Delta S_{298,act}$	Activation entropy	$i_{a,p}$	Current density of oxide dissolution
$\Delta H_{298,act}$	Activation enthalpy	ψ	Applied potential
H_{Corr}	Enthalpy correction	i^*	Concentration-independent part of exchange current density
$-TS_{298}$	Entropy correction	C^s	Species concentration around the electrode surface
$E_{298(0K)}$	Zero-point energy	ω	Reaction order
k_B	Boltzmann's constant	E^0	Reversible potential
h	Planck's constant	α	Electrochemical transfer coefficient
T	Temperature	M_m	Metal molecular weight
R_g	Gas constant	ρ_m	Density
C	Species concentration	z_m	Effective valence
\vec{N}_j	Flux density for dilute solution	\vec{n}	Outward-pointing unit normal vector on the electrolyte domain
R_j	Reaction rate of reaction j	$i_{c,m}$	Metal-ion-reduction component of total cathodic current density
D	Diffusion coefficient is the	C_j^∞	Bulk concentration of species j
z	Charge number	$i_{e-m,j}$	Current density resulting from an electrochemical reaction involving species j

1. Introduction

Light-weight aluminum alloys with excellent mechanical properties have been extensively used in defense and aerospace applications. Yet, these alloys are prone to localized pitting corrosion, which often takes place on the surface of passivated metals with a native oxide layer, due to the presence of heterogeneous microstructures [1, 2]. When aggressive anions (e.g., Cl^-) attack aluminum alloys, severe localized pits with sizes ranging from nano- to millimeters can form, which are difficult to diagnose and frequently initiate cracks that eventually lead to catastrophic failures [3]. The complexity of this issue is primarily due to two factors: the microstructure of the alloy and the corrosion environment, both of which vary dynamically with time and exhibit significant heterogeneity [4].

Aluminum alloys possess complex microstructures due to the presence of intermetallic particles (IMPs) with a broad range of compositions and sizes, as well as periphery phases around composite particles and clustering [5]. The IMPs, which have a variety of compositions and phases, are believed to be critical sites for the initiation of localized corrosion due to particle dealloying, etching of the alloy matrix, and Cu redistribution on

the surface [6, 7]. The latter phenomena drastically alter the local electrochemical activity on the surface of aluminum alloys, hastening the progression of localized pitting corrosion [8, 9]. Extensive efforts have been made to characterize the electrochemical and dissolution behaviors, such as pitting potential, corrosion potential, and polarization curves, of all forms of IMPs (e.g., Al₂Cu and Al₂CuMg) within aluminum alloys under various corrosion environments [10-16]. These studies demonstrated that the local corrosion environment governs the main phenomena at the alloy-solution interface, such as IMP dealloying, aluminum oxide formation and dissolution, matrix etching, and Cu redistribution. Moreover, pit morphology, electrical potential, electrolyte chemistry, and microstructure of aluminum alloys, all of which are space-time variant features, exhibit coupled effects on localized pitting corrosion. However, differentiating the effects of each individual feature on pitting corrosion through experiments is very challenging. In particular, the distinct role of galvanic coupling and electrolyte chemistry in the initiation and propagation of localized pits around copper-rich IMPs still need investigations [17].

In order to improve the corrosion performance of aluminum alloys, numerous surface modification techniques, such as organic (or polymeric), inorganic (e.g., anodization, conversion coating, physical or chemical vapor deposition, and electroplating), and hybrid organic-inorganic coatings (e.g., sol-gel coating), have been broadly investigated [18]. Conversion coating is used as a stronger pretreatment coating in a variety of coating applications. Chromate conversion coatings (CCCs) are the most important coatings used in a wide range of applications in the aircraft and defense industries due to their exceptional corrosion performance and great adhesion properties [19]. CCCs are chromium compounds in the 6+ oxidation state that provide self-healing corrosion inhibition due to the reduction of Cr(VI) within the coating to insoluble Cr(III) compounds [20]. The ability of such coatings to reform a Cr-containing protective barrier after the CCC layer is broken during the chemical process is referred to as self-healing.

Yet, recent studies have shown that hexavalent chromium poses significant environmental and health hazards [21, 22]. CCCs threaten workers' life due to the high degree of toxicity and carcinogenicity of chromate compounds, thus their usage is largely prohibited within the United States (by the Occupational Safety and Health Administration) and the European Union (by the Restriction of Hazardous Substances Directive). These issues have motivated researchers to develop chromate-free conversion coatings with equal or better corrosion performance over the last two decades [23-26]. Several chromate-free conversion coatings, including rare-earth metal (REM), Ti, and Zr-based coatings, have been introduced to improve the corrosion performance of aluminum alloys. Among these alternatives, Zr-based conversion coating (ZrCC) has the advantages of having a low environmental impact while also being abundant and economically viable [27-29]. Extensive experimental efforts have been devoted to improving corrosion performance of ZrCC for aluminum alloys [24, 26, 30-34]. However, development of an effective ZrCC for long-term corrosion prevention requires a thorough understanding of the underlying interfacial kinetics and surface chemistry, as well as optimization of coating formulations and compositions. Since characterizing the above-mentioned space-time variant features is experimentally very challenging, multiscale modeling and simulations offer chemo-physics-based tools for investigating the controlling factors for corrosion prevention.

To date, various modeling approaches, including finite element method (FEM) and first-principles, have been reported to investigate corrosion of metallic materials such as steel (or iron), magnesium, and aluminum alloys [3, 4, 17, 35-51]. Aiming at energetic calculation and phase stability evaluation, *ab initio* was used to investigate surface phenomena such as dissolution, adsorption, and oxygen reduction reaction with metal/alloy at the nanoscale [52, 53]. Yet, such simulations are limited to very small systems that cannot properly describe the localized pitting process and dynamics related to those phenomena, all of which may take months or years. FE

models, on the other hand, have been widely used for corrosion studies of different materials due to the ability to simulate localized pits with real-world dimensions and environmental conditions. However, according to Xiao and Chaudhuri [4], most of these models were developed based on simple and fixed pit geometry and simplified solution chemistry, with critical assumptions such as zero concentration gradient in electrolyte and time-invariant interfacial kinetics. Furthermore, they used simple metal compositions, which are inapplicable to aluminum alloys with heterogeneous microstructures and compositions [4, 5]. Current FE models rely heavily on experimental-based corrosion mechanism parametrization, and thus the availability of sufficient and accurate experimental data severely limits the predictability of such models.

Incorporating first-principles into a multiscale modeling framework is believed to significantly improve predictive corrosion models [4, 54]. Yet, to the best of our knowledge, no multiscale modeling has been conducted on the localized pitting corrosion of light-weight alloys coated with conversion coatings. This work develops a multiscale model that fully describes the coupled effects of electrolyte chemistry, interfacial kinetics, alloy microstructure, and pit morphology on the corrosion rate and stability of pits. Using density functional theory (DFT) and FEM, this model explores the interrelationships between these features to promote a fundamental understanding of localized pitting corrosion in aluminum alloys with Zr-based conversion coatings. The proposed kinetic model for electrolyte and surface chemistry was completed using DFT and transition-state theory. This research focuses on the propagation and repassivation of a localized pit in vicinity of a cathodic IMP. This work contributes to reducing the number of unknown parameters for underlying reaction mechanisms and hastening the development of more comprehensive models for corrosion resistance of conversion coatings. Section 2 will present a generic multiscale modeling framework with details of the DFT calculations and multiphysics model, Section 3 will discuss the results, and Section 4 will summarize the implications of this research.

2. Multiscale Modeling of Localized Corrosion

Figure 1 shows the system investigated in this work, which involves the exposure of an aluminum alloy to a sodium chloride (NaCl) solution. The alloy microstructure was obtained from SEM images [55] to serve as model geometry for simulations that mimics a real system. The SEM image, shown in **Figure S3.3**, is associated with a scribed coated aluminum alloy panel exposed to 0.01 M NaCl neutral solution for 100 hours of salt fog testing. The model considers a system comprised of a pure aluminum matrix and an IMP region, i.e., θ -phase (Al_2Cu). Note that this is a simulation of a damaged spot such as a scribed panel that can expose the IMPs. Two layers of metal oxides protect the Al matrix: a thin inner layer of native aluminum oxide (Al_2O_3) and a thick deposited layer of zirconium oxide (ZrO_2). This study focuses on pit propagation and repassivation near a cathodic IMP, with repassivation triggered by the formation of a passive layer of aluminum oxide and other insoluble precipitates on the surface [13, 14]. The model considers four main domains, as shown in **Figure 1(a)**: aluminum matrix Ω_{Al} as anode, θ -phase (Al_2Cu) Ω_θ as cathode, passive oxide layer (i.e., including both Al_2O_3 and ZrO_2 layers) Ω_p , and electrolyte (NaCl solution) Ω_e . The solid-liquid interface is defined as $\partial\Omega_{e-m} = \partial\Omega_e \cap (\partial\Omega_{Al} \cup \partial\Omega_\theta \cup \partial\Omega_p)$.

Figure 1(b) presents a generic multiscale modeling framework for investigating localized corrosion in light-weight alloys. It includes three layers of modeling blocks that are distinguished by their dependencies and relationships with one another and are linked to an experimental data block. The modeling process starts with inputs from experimental data such as pit surface geometry and corrosion environment. In the first modeling layer, first-principles and transition state theory are used to calculate required thermodynamic parameters, including internal energy, enthalpy, and Gibbs free energy of activation for electrochemical reactions. The

Eyring-Polanyi relation, which will be explained in the following section, aids in obtaining rate constants for dissolution reactions in order to complete the kinetics model. The reaction kinetics serves as an input in the second layer, where the mass transport model is coupled with electrochemical reactions to characterize the chemical (i.e., material concentrations) and electrical (i.e., electrostatic potential) environments. In the third layer, the corrosive environment is used to determine both reactive species fluxes through the solid-liquid interface and changes in interface location. Subsequently, the pit boundary location and condition for the specified electrolyte model are obtained.

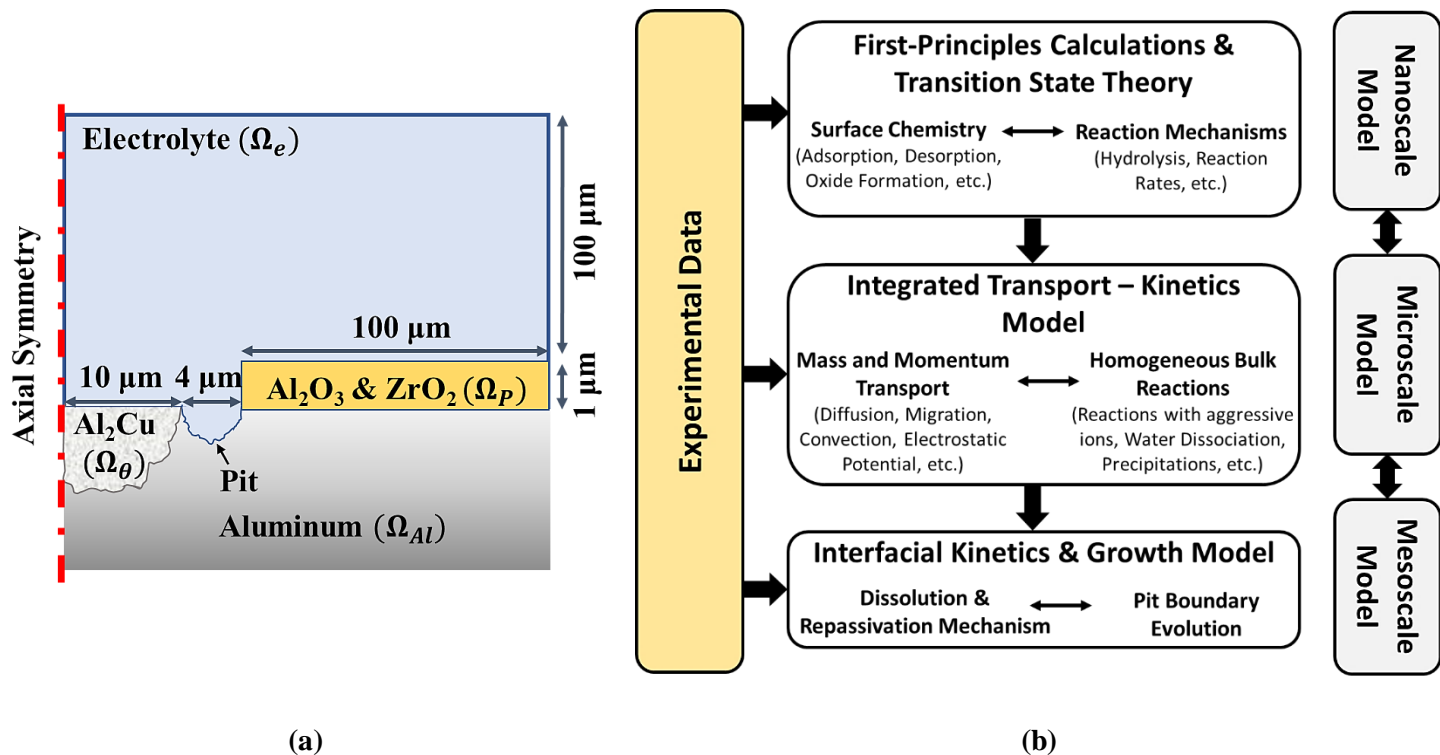


Figure 1: (a) Schematic showing the geometry used for corrosion models. A pit is located adjacent to the cathodic region, which is composed of Al_2Cu IMPs (θ -phase). A layer of Zr-based conversion coating covers the aluminum matrix, beneath which is a very thin layer of native alumina. The coating layer has a thickness of 1 μm . The models incorporate real-world pit geometry. The electrolyte is a sodium chloride (NaCl) solution. (b) The scheme for multiscale modeling of localized corrosion of alloys/metals. First-principles in conjunction with transition-state theory are used for energetic calculations to eventually determine the values of reaction parameters (e.g., barrier energy and rate constants). Coupling the proposed kinetics with a mass transport model, the corrosive environment over the alloy is determined. Finally, the growth of pit and its stability are quantitatively predicted.

2.1 First-Principles Calculations

Among the various mechanisms for metal hydrolysis reaction in aqueous solution reported in the literature, this work used the reaction pathway for first-order hydrolysis introduced by Dong et al. [56]. The steps for calculating the energy barrier of reactions are explained as follows in this work. In the first step, the initial and final images, as their coordinates are provided in the supplementary document, were constructed. Next, density functional theory (DFT) calculations were performed to obtain the energies and forces, which are originated due to the potential energy surface (PES), acting on the system of atoms (or the images).

We used Quantum Espresso (QE) package [57] with non-conserving pseudopotential. The exchange correlation functional was approximated by generalized gradient approximation (GGA) in the formulation of PBE (Perdew-Burke-Ernzerhof) [58]. The wave function in QE was expanded through plane waves up to energy of 50 Rydberg. In the next step, climbing image – nudged elastic band (CI-NEB) method was used to determine the reaction pathways [59, 60]. This method works through converging a trial initial path in the PES to the

minimum energy pathway (MEP) near the initial path [61]. The number of images used to construct the path determines its resolution. CI-NEB, despite the basic NEB method, forces one of the images to have the highest PES [61]. Finally, interpolating over converged images provided the energy barrier.

All DFT calculations were carried out at 0 K. Supplementary information includes the Cartesian coordinates of all reaction species for reactants and transition states. The electronic energies $E_{Elec(0K)}$ for aqueous reaction species were computed using DFT calculations. Subsequently, the thermodynamic variables total energy E_{298} , Gibbs free energy G_{298} , and enthalpy H_{298} for those species were obtained by adding enthalpy correction H_{Corr} , entropy correction $-TS_{298}$, and zero-point energy $E_{298(0K)}$ onto $E_{Elec(0K)}$ [62]. The zero-point energy can be obtained from frequency calculations. H_{Corr} , E_{298} , and $-TS_{298}$ are determined using thermochemistry analyses carried out at 1 atm and 298.15 K. The Eyring equation yields the transition-state rate constant:

$$k_{TST} = \frac{k_B T}{h} \cdot \exp\left(-\frac{\Delta G_{298,act}}{R_g T}\right) = \frac{k_B T}{h} \cdot \exp\left(-\frac{\Delta S_{298,act}}{R_g T} - \frac{\Delta H_{298,act}}{R_g T}\right) \quad (1)$$

where k_B , h , T , R_g , $\Delta G_{298,act}$, $\Delta S_{298,act}$, and $\Delta H_{298,act}$ denote the Boltzmann's constant, Planck's constant, temperature, gas constant, activation Gibbs free energy at 298 K, activation entropy, and activation enthalpy, respectively.

2.2 Multiphysics Model

The multiphysics model used in this work is similar to one introduced and detailed previously by Xiao and Chaudhuri [4]. The following explains its key features, including certain variations in reaction kinetics compared to the one presented in [4].

2.2.1 Material Balance

Both mass transport and reaction kinetics have a direct impact on the dynamical changes in mass for each chemical species j in the electrolyte solution, which can be expressed mathematically as follows:

$$\frac{\partial C_j}{\partial t} = -\nabla \cdot \vec{N}_j + R_j \quad (2)$$

where C , \vec{N} , and R represent the concentration (mol/m^3), flux density ($mol/(m^2s)$), and reaction rate ($mol/(m^3s)$), respectively. Since species mass transfer is driven by differences in electrical or chemical potential between two sites in an aqueous solution, the flux density \vec{N} for the dilute solution can be expressed in terms of convection, migration, and diffusion:

$$\vec{N}_j = -D_j \nabla C_j - z_j F \frac{D_j}{R_g T} C_j \nabla \varphi + C_j \vec{v} \quad (3)$$

where D is the diffusion coefficient (m^2/s); z is the charge number; R_g is the gas constant ($8.314 J/(mol K)$); φ denotes the electrostatic potential (V); and \vec{v} is the flow velocity, which is zero in the case of a stagnant electrolyte solution.

The general form of the chemical production or consumption rate can be given as [63]

$$R_j = \sum_{m=1}^{N^r} \left\{ -\omega_j^m \left(k_f^m \prod_{\forall \omega_l^m > 0} (C_l)^{\omega_l^m} - k_b^m \prod_{\forall \omega_l^m < 0} (C_l)^{-\omega_l^m} \right) \right\} \quad (4)$$

where N^r , ω_l^m , k_f^m , and k_b^m are the total number of reactions, the stoichiometric coefficient of species l in the m th reaction, the forward reaction rate constant, and the backward reaction rate constant, respectively. For reaction products, the stoichiometric coefficient is negative, while for reactants, it is positive. Historically, all homogeneous bulk reactions were assumed to be in equilibrium at any given position in solution and time [3, 4, 41, 45, 55]. This assumption is avoided in our work because it could lead to significant errors in calculating chemical species concentrations at high dissolution current densities [3].

The electroneutrality condition given below allows us to solve [equation \(2\)](#) to obtain both the electrostatic potential and the species concentration for the dilute solution:

$$\sum_j z_j C_j = 0 \quad (5)$$

2.2.2 Surface Reaction Mechanism

This section focuses on interfacial phenomena so that interfacial kinetics, material-solution chemistry, and surface morphology can be mathematically correlated.

2.2.2.1. Anodic Kinetics

The pit state transition resulting from rivalry between passive oxide layer formation and dissolution (of aluminum in our case) is used in this multiphysics model [4, 64]. The total current density (A/m^2) associated with the anode can be expressed as follows:

$$i_a = (i_{a,1} + i_{a,2})(1 - \theta_0) \quad (6)$$

where $i_{a,1}$ and $i_{a,2}$ denote the magnitudes of active dissolution and oxide formation (of aluminum in this study) current densities, respectively. θ_0 is the oxide coverage fraction:

$$\theta_0 = \frac{i_{a,2}}{i_{a,2} + i_{a,p}} \quad (7)$$

in which $i_{a,p}$ is the current density of oxide dissolution. Based on Anderko et al. [65], adsorption of aggressive and inhibitive species is respectively responsible for active dissolution and oxide formation (of aluminum). The current densities in [equation \(6\)](#) can be quantitatively correlated to temperature T , electrostatic potential φ , applied potential ψ , electrolyte chemistry, and materials as expressed below [4, 64]:

$$i_{a,1} = \sum_j i_{1,j}^* (C_j^s)^{\omega_j} \cdot \exp\left(\frac{\alpha_j F (\psi - \varphi - E_{M,j}^0)}{R_g T}\right) \quad (8)$$

$$i_{a,2} = \sum_j i_{2,j}^* (C_j^s)^{\omega_j} \cdot \exp\left(\frac{\alpha_j F (\psi - \varphi - E_{Mo,j}^0)}{R_g T}\right) \quad (9)$$

where i^* , C^s , and ω are the concentration-independent part of exchange current density [64], species concentration around the electrode surface [65], and reaction order, respectively. E^0 and α are the reversible potential and electrochemical transfer coefficient, respectively. The subscript j represents an aggressive ion for $i_{a,1}$ and an inhibitive ion for $i_{a,2}$. The reaction kinetics, which is strongly dependent on the solution chemistry, can be written as:

$$i_{a,P} = \sum_j k_{P,j} (C_j^s)^{\omega_j} \quad (10)$$

The corrosion rate can be obtained from the following relationship:

$$R_{Corr} = \frac{M_m}{z_m F} \frac{\int_{\partial\Omega_{e-a}} i_a dS}{\int_{\partial\Omega_{e-a}} dS} \quad (11)$$

in which $\partial\Omega_{e-a} = \partial\Omega_a \cap \partial\Omega_{e-m}$.

2.2.2.2 Cathodic Kinetics

The general format of the kinetic expression for electrochemical reduction reactions on cathodes is as follows:

$$i_c = - \sum_j i_{c,j}^* (C_j^s)^{\omega_j} \cdot \exp\left(-\frac{\alpha_j F (\psi - \phi - E_j^0)}{R_g T}\right) \quad (12)$$

where the subscript j represents a dissolved ion to be reduced.

2.2.2.3 Interface Boundary Evolution

The following relation can be used to track the position of the solid-liquid interface, Λ , during pit growth:

$$\frac{\partial \vec{\Lambda}}{\partial t} = -i_{e-m,m} \frac{M_m}{\rho_m z_m F} \vec{n} \quad \forall \vec{\Lambda} \in \partial\Omega_{e-m}(t) \quad (13)$$

where M_m , ρ_m , z_m , and \vec{n} denote the metal molecular weight, density, effective valence, and outward-pointing unit normal vector on the electrolyte domain, respectively. $i_{e-m,m}$ can be determined using the following function, which is time and location dependent:

$$i_{e-m,m} = \begin{cases} i_a & \forall \vec{\Lambda} \in \partial\Omega_a(t) \cap \partial\Omega_{e-m}(t) \\ i_{c,m} & \forall \vec{\Lambda} \in \partial\Omega_c(t) \cap \partial\Omega_{e-m}(t) \\ 0 & \forall \vec{\Lambda} \in \partial\Omega_p(t) \cap \partial\Omega_{e-m}(t) \end{cases} \quad (14)$$

where $i_{c,m}$ denotes the metal-ion-reduction component of total cathodic current density [4]. According to [Equations \(13\) and \(14\)](#), i_a determines the speed at which the pit propagates through the anode. There is no material transfer between the oxide layer (ZrO_2) and electrolyte solution. Note that we have a native oxide passivation mechanism for alumina to recalculate the exposed metal surface and oxide covered area in the pit.

2.2.2.4 Initial and Boundary Conditions

The multiphysics model is based on mass transport phenomena in electrolytes with moving pit boundaries. In this study, the following relationships were considered for the initial conditions:

$$C_j(\vec{\Lambda}, t = 0) = C_j^\infty \quad \forall \vec{\Lambda} \in \Omega_e \quad (15)$$

$$\varphi(\vec{\Lambda}, t = 0) = \varphi^\infty \quad \forall \vec{\Lambda} \in \Omega_e \quad (16)$$

in which C_j^∞ and φ^∞ denote the bulk concentration of species j and the electrostatic potential, respectively. Other conditions that can be applied to the boundaries far from the pit are as follows:

$$C_j(\vec{\Lambda}, t > 0) = C_j^\infty \quad \forall \vec{\Lambda} \in \partial\Omega_e / \partial\Omega_{e-m} \quad (17)$$

$$\varphi(\vec{\Lambda}, t > 0) = \varphi^\infty \quad \forall \vec{\Lambda} \in \partial\Omega_e / \partial\Omega_{e-m} \quad (18)$$

While the initial boundary $\partial\Omega_{e-m}(t = 0)$ is associated with the surface morphology obtained from experiments, equations (13) and (14) determine the boundary location $\partial\Omega_{e-m}(t > 0)$ during the corrosion process. The flux of chemical species involved in interfacial reactions can be obtained using the following relationship:

$$\vec{N}_j(\vec{\Lambda}, t > 0) = \frac{-i_{e-m,j}}{z_j F} \vec{n} \quad \forall \vec{\Lambda} \in \partial\Omega_{e-m} \quad (19)$$

where $i_{e-m,j}$ denotes the current density resulting from an electrochemical reaction involving species j (see equation (14) to obtain this term).

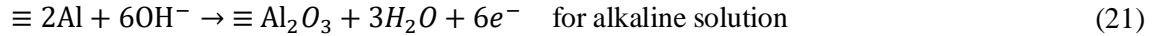
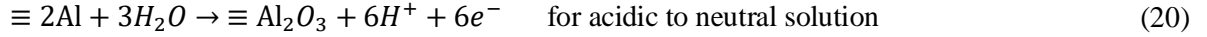
3. Case Study: Aluminum Alloy with Zr-Based Conversion Coating

In this work, the presented multiscale modeling approach was used to investigate localized pitting corrosion in aluminum alloys coated with a zirconia layer and immersed in NaCl solution (Figure 1(a)). To better understand the critical phenomena that occur during corrosion, some assumptions were considered in order to simplify the current problem. The following are the assumptions: 1) dealloying of Al₂Cu is inhibited by covering a passive layer on the θ -phase, as found in experiments [12], 2) Cu-plating on the θ -phase is ignored after covering this phase with an insoluble CuCl passive layer, 3) the zirconia layer (i.e., Ω_p) remains intact during the simulations, and 4) Al(OH)₃ precipitation as a corrosion product on the pit is ignored due to its low concentration when $pH < 4$ [3]. Because of hydrolysis reactions, the solution in an active pit is very acidic [66].

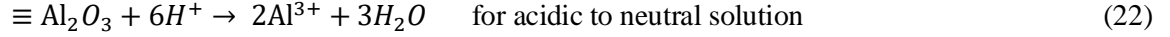
3.1 Reaction Mechanisms

The kinetics model associated with the localized corrosion of an aluminum alloy coated with a zirconia layer consists of homogeneous bulk reactions involving both Al and Zr species. Table 1 contains a list of these reactions (reactions 1-16), which were compiled from various works of literature. It should be noted that the model does not account for reactive dissolution of ZrO₂ in the vicinity of a pit. The coating is considered to be responsible for the excess Zr⁴⁺. The processes in ZrO₂ are very complex, including multistep dissolution and hydroxide formation. It is only used for native zirconium alloys.

In anodic region, a layer of oxide film can form as a result of the following reactions, which causes repassivation of the active pit in aluminum alloys:



On the other hand, dissolution reactions of the oxide film at different pH levels are as follows:



In the cathodic region, however, oxygen reduction is assumed to be the only cathodic reaction on the Cu surface:



3.2 Simulation Inputs

The material properties used in the modeling for aluminum and zirconium are: $M_{w,Al6061} = 26.98 \text{ g/mol}$, $\rho_{Al6061} = 2700 \text{ kg/m}^3$, $M_{w,Zr} = 91.22 \text{ g/mol}$, and $\rho_{Zr} = 6506 \text{ kg/m}^3$. The following dissolved species were considered in the simulations: Zr^{4+} , ZrO^{2+} , $ZrOH^{3+}$, $Zr(OH)_2^{2+}$, $ZrCl^{3+}$, $Zr(OH)Cl^{2+}$, $ZrOCl^+$, $Zr(OH)_3Cl$, $ZrO(OH)Cl$, Al^{3+} , $Al(OH)^{2+}$, $Al(OH)_2^+$, $Al_2(OH)_2^{4+}$, $AlCl^{2+}$, $Al(OH)Cl^+$, $Al(OH)_2Cl$, Cl^- , H^+ , OH^- , Na^+ , and O_2 . The diffusion coefficients for these species were collected from the literature [3, 67]. The diffusion coefficient for Zr-containing species was considered to be the same and equal to $2.36 \times 10^{-11} \text{ m}^2/\text{s}$ [67]. The diffusion coefficient was calculated by extrapolating the curve for the variation of applied current versus time for different temperatures provided in [67].

The component was immersed in a NaCl solution at room temperature, 298.15 K. The concentration of the solution was considered to have a range from 10^{-4} M to 1 M . A bulk concentration of $60 \mu\text{M}$ was set for the dissolved oxygen in the electrolyte [68]. The applied potentials were changed from -1 V to -0.55 V (vs. saturated calomel electrode (SCE)). Note that this study aims at investigating the full anodic polarization behavior by changing the applied potentials. Furthermore, the free corrosion case, in which the applied potentials equal the open circuit potential (OCP), is not explored.

The parameter values for Butler-Volmert equation used for the electrode kinetics were collected from literature [3, 4]. The exchange current densities were considered to be the same and equal to 10^{-5} A/m^2 for both oxide formation and active dissolution. The current densities for passive and cathodic dissolutions were set as 10^{-2} A/m^2 and 10^{-4} A/m^2 , respectively. The mechanism of cathodic dissolution of aluminum involves alkalization of the oxide/solution or aluminum/solution interfaces during oxygen and water reduction, which results in chemical dissolution of the oxide or metal [69-71]. The values of applied potential and reversible potentials for aggressive species and inhibitive species were considered as -0.5 V , -0.911 V , and -0.4 V , respectively. The reversible potential for dissolved species in cathode was set as -0.282 V . In this study, the electrochemical transfer coefficient α is set to 0.7.

4. Results and Discussion

4.1 Evaluation of Kinetics and Multiscale Models

To complete the kinetics model for multiphysics simulations, DFT-TST calculations were carried out to determine the missing reaction constants and energy barriers for first-order reactions involving Zr. However, reaction constants for a few reactions containing Al were obtained for evaluating the calculations due to a lack of experimental data for the rate constants and energy barriers of Zr-containing reactions. **Table 1** shows the results of calculations that include the forward-reaction rate constant and the energy barrier. Comparisons of computed and experimental values for the kinetic parameters indicate that for reactions containing Al, calculations overestimated the rate constants by less than 50%. However, the results of the calculations may fall within the measurement error, which has not been reported in the literature. In addition, the difference in reaction rate constants between experiments and DFT-TST calculations can be attributed to the variation of conditions under which the data are obtained [72]. The rate constants used in the simulations are a combination of data from both experiments and DFT-TST calculations, as shown in the last two columns of **Table 1**. Due to very expensive computations, the values for the second-order reaction rates containing Zr were assumed in this study.

To assess the multiscale models, the corrosion rates of bare aluminum and zirconium obtained from simulations were compared to the experimental results in **Table 2**. In general, the model is about zirconia coated Al-6061 and the Zr 705/702 are reference for the oxide layer. Al_2Cu is a cathodic impurity in Al-6061, which is used in the model for driving galvanic corrosion. Note that the only metal corroding in this paper is Al-6061. The kinetic model for the bare aluminum includes reactions (4-6), (9,10), and (14-16), reported by Guseva et al. [3]. The reactions (1-3), (7,8), (11-13), and (16) are considered for the kinetic model of Zr 705/702. The parameter values input for the three materials compared in **Table 2** differ only in that the reactions considered in the kinetic model differ in these cases. The simulation inputs were set to match the experimental conditions. Model results are in good agreement (almost in the same ballpark) with measurements reported in the literature. Differences in corrosion rates between simulations and experiments can be explained by differences in the conditions under which the data is obtained. Along with the results for Al 6061 and Zr 705/702, the corrosion rate of Al 6061 with Zr-based conversion coating is reported for the same conditions as bare Al 6061 to better understand the effects of Zr-based coatings on the corrosion performance of aluminum alloys. However, there is no experimental data for Al coated with ZrO_2 in the literature. According to the simulation results in **Table 2**, Zr-based conversion coating improves the corrosion performance of aluminum alloys immersed in NaCl solution, which is in line with experimental findings [19, 73-75]. The reasons will be explained in the following section.

Table 1: Homogeneous bulk reactions proposed for the dissolution of aluminum alloy with Zr-based conversion coating immersed in chloride solution. The energy barrier ΔG and rate constants for forward reaction K_f and backward reaction K_b is used to compare DFT calculations performed in this work with experimental data. The rate constants selected for experiments are a combination of experimental and DFT data.

Reaction Type	Reaction	DFT – Transition State Theory		Experiment			Selected Rate Constants for Simulations	
		ΔG (Cal/mol)	K_f	K_f	K_b	Ref. ^a	K_f	K_b
Hydrolysis	$Zr^{4+} + H_2O \leftrightarrow ZrOH^{3+} + H^+$ (1)	1.37×10^4	$4.49 \times 10^2 \text{ s}^{-1}$	-	-	[76, 77]	$4.49 \times 10^2 \text{ s}^{-1}$	$1 \times 10^7 \text{ M}^{-1} \text{ s}^{-1} \text{ }^c$
	$Zr^{4+} + H_2O \leftrightarrow ZrO^{2+} + 2H^+$ (2)	2.53×10^4	$1.24 \times 10^{-6} \text{ s}^{-1}$	-	-	[78]	$1.24 \times 10^{-6} \text{ s}^{-1}$	$1 \times 10^2 \text{ M}^{-1} \text{ s}^{-1} \text{ }^c$
	$ZrOH^{3+} + H_2O \leftrightarrow Zr(OH)_2^{2+} + H^+$ (3)	7.81×10^3	$1.01 \times 10^7 \text{ s}^{-1}$	-	-	[76]	$1.01 \times 10^7 \text{ s}^{-1}$	$1 \times 10^9 \text{ M}^{-1} \text{ s}^{-1} \text{ }^c$
	$Al^{3+} + H_2O \leftrightarrow Al(OH)^{2+} + H^+$ (4)	1.03×10^4	$1.58 \times 10^5 \text{ s}^{-1}$	$1.09 \times 10^5 \text{ s}^{-1}$	$4.4 \times 10^9 \text{ M}^{-1} \text{ s}^{-1}$	[79]	$1.09 \times 10^5 \text{ s}^{-1}$	$4.4 \times 10^9 \text{ M}^{-1} \text{ s}^{-1}$
	$Al(OH)^{2+} + H_2O \leftrightarrow Al(OH)_2^+ + H^+ \text{ }^c$ (5)	6.89×10^3	$4.87 \times 10^7 \text{ s}^{-1}$	-	-	[3]	$4.87 \times 10^7 \text{ s}^{-1}$	$4.4 \times 10^9 \text{ M}^{-1} \text{ s}^{-1} \text{ }^c$
	$2Al^{3+} + 2H_2O \leftrightarrow Al_2(OH)_2^{4+} + 2H^+$ (6)	-	-	$10^{-2} \text{ M}^{-1} \text{ s}^{-1}$	$10^8 \text{ M}^{-1} \text{ s}^{-1}$	[79]	$10^{-2} \text{ M}^{-1} \text{ s}^{-1}$	$10^8 \text{ M}^{-1} \text{ s}^{-1}$
Reactions with Cl ⁻ ion	$Zr^{4+} + Cl^- \leftrightarrow ZrCl^{3+}$ (7)	-	-	-	-	[80]	$100 \text{ M}^{-1} \text{ s}^{-1} \text{ }^c$	$10 \text{ s}^{-1} \text{ }^c$
	$ZrOH^{3+} + Cl^- \leftrightarrow Zr(OH)Cl^{2+}$ (8)	-	-	-	-	[80]	$10 \text{ M}^{-1} \text{ s}^{-1} \text{ }^c$	$1000 \text{ s}^{-1} \text{ }^c$
	$Al^{3+} + Cl^- \leftrightarrow AlCl^{2+}$ (9)	-	-	$226 \text{ M}^{-1} \text{ s}^{-1}$	$75 - k_f \cdot (c_{Al^{3+}} - c_{AlOH^{2+}}) \text{ s}^{-1}$	[81]	$226 \text{ M}^{-1} \text{ s}^{-1}$	$75 - k_f \cdot (c_{Al^{3+}} - c_{AlOH^{2+}}) \text{ s}^{-1}$
	$Al(OH)^{2+} + Cl^- \leftrightarrow Al(OH)Cl^+$ (10)	-	-	$19 \text{ M}^{-1} \text{ s}^{-1}$	$5700 - k_f \cdot c_{AlOH^{2+}} \text{ s}^{-1}$	[81]	$19 \text{ M}^{-1} \text{ s}^{-1}$	$5700 - k_f \cdot c_{AlOH^{2+}} \text{ s}^{-1}$

Product Formation	$\text{ZrCl}^{3+} + 3\text{H}_2\text{O} \rightarrow \text{Zr(OH)}_3\text{Cl} + 3\text{H}^+$ (11)	2.19×10^4	$3.62 \times 10^{-4} \text{ s}^{-1}$	-	-	b	$3.62 \times 10^{-4} \text{ s}^{-1}$	-
	$\text{Zr(OH)Cl}^{2+} + 2\text{H}_2\text{O} \rightarrow \text{Zr(OH)}_3\text{Cl} + 2\text{H}^+$ (12)	2.17×10^4	$5.26 \times 10^{-4} \text{ s}^{-1}$	-	-	b	$5.26 \times 10^{-4} \text{ s}^{-1}$	-
	$\text{ZrOCl}^+ + \text{H}_2\text{O} \rightarrow \text{ZrO(OH)Cl} + \text{H}^+$ (13)	2.52×10^4	$1.44 \times 10^{-6} \text{ s}^{-1}$	-	-	b	$1.44 \times 10^{-6} \text{ s}^{-1}$	-
	$\text{AlCl}^{2+} + 2\text{H}_2\text{O} \rightarrow \text{Al(OH)}_2\text{Cl} + 2\text{H}^+$ (14)	2.43×10^4	$5.94 \times 10^{-6} \text{ s}^{-1}$	$4 \times 10^{-6} \text{ s}^{-1}$	-	[82]	$4 \times 10^{-6} \text{ s}^{-1}$	-
	$\text{Al(OH)Cl}^+ + \text{H}_2\text{O} \rightarrow \text{Al(OH)}_2\text{Cl} + \text{H}^+$ (15)	2.10×10^4	$1.74 \times 10^{-3} \text{ s}^{-1}$	$4 \times 10^{-6} \text{ s}^{-1}$ c	-	[82]	$4 \times 10^{-6} \text{ s}^{-1}$	-
Water Dissociation	$\text{H}_2\text{O} \leftrightarrow \text{OH}^- + \text{H}^+$ (16)	2.32×10^4	$4.37 \times 10^{-5} \text{ s}^{-1}$	$2.6 \times 10^{-5} \text{ s}^{-1}$	$1.3 \times 10^{11} \text{ M}^{-1} \text{ s}^{-1}$	[83]	$2.6 \times 10^{-5} \text{ s}^{-1}$	$1.3 \times 10^{11} \text{ M}^{-1} \text{ s}^{-1}$

^a References are associated with both reactions and experimental data for reaction constants.

^b Reactions are proposed in this study.

^c Assumed.

Table 2: Corrosion rate of bare aluminum alloy 6061, bare zirconium 705/702, and aluminum alloy 6061 with Zr-based conversion coating obtained from simulations in this work and reported experimental measurements. Certain conditions for simulations and experimental measurements are also mentioned for the purpose of comparison.

Metal	Simulations		Experiment		
	Condition	R_{Corr} (mm/year)	Condition	R_{Corr} (mm/year)	Ref.
Al 6061	NaCl, 30 °C, pH = 6, Steady	0.020899	NaCl (1%), 30 - 50 °C, pH = 5.8 – 6.0, after 480 hr	0.0305	[84]
Zr 705/702	NaCl, 30 °C, pH = 1, Steady	0.0005506	NaCl (25%), 35-100 °C, pH = 1, after 504 hr	< 0.0007	[85, 86]
Al with ZrO ₂ Coating	NaCl, 30 °C, pH = 6, Steady	0.002254	NaCl, 30 °C, pH = 6.5 – 7.2	0.005588 ± 0.0038	[87]

4.2 Environmental Effects on the Growth of Pit

To understand the effects of chloride ions (i.e., Cl^-) as aggressive species on localized pitting corrosion, the change in corrosion rate of bare Al 6061, bare Zr 705, and Al 6061 coated with Zr-based conversion coating as a function of the bulk concentration of chloride ions in the solution is plotted in [Figure 2\(a\)](#). Here, the alloy was immersed in a neutral NaCl solution and was potentiostatically controlled with a $-0.55 V$ applied potential. A fixed pit geometry corresponding to a particular instant of time during pit propagation was used. The figure shows that the corrosion rate of the systems increases as the bulk concentration of Cl^- was increased. This is because increasing the bulk concentration of Cl^- in the solution drives more chloride ions to the pit surface, resulting in increased acidity in the pit (see [Figure 2\(b\)](#)) and thus increased corrosion rate of the system. Experimental observations for localized corrosion of aluminum alloys indicated the same pattern [88].

Furthermore, [Figure 2\(a\)](#) demonstrates that Zr-based conversion coatings promote the corrosion resistance of aluminum alloys due to the involvement of Zr in interfacial kinetics. This is due to the suppression of both the oxygen reduction reaction (ORR) and anodic dissolution, with the ORR being more strongly inhibited than bare Al 6061 due to the impediment of oxygen chemisorption on IMPs [89]. It is worth mentioning that the oxygen concentrations deplete in the pit due to all chemical reactions, leading to the difficulty in repassivation (see the oxygen concentration contour plot on the Supplementary document). The corrosion rate of Zr is very low in comparison to the other two systems. The latter is due primarily to the fact that the anodic current density (as defined in the Anodic Kinetic section) is influenced by the reactions and their rates of reaction. The kinetic models of coated and bare Al differ in terms of reaction within the pit, which influences corrosion rates.

[Figure 2\(b\)](#) depicts the pH distribution along the pit surface, specifically close to the solid-liquid interface. With a constant pH, the pit status changes from active to passive as the concentration of Cl^- in the solution decreases, which is in line with the experimental observations [90]. Note that the pH changes over the pit surface even for dilute concentration of Cl^- (e.g., $10^{-4}M$ and $10^{-3}M$), which cannot be observed from [Figure 2\(b\)](#). We

specifically added [Figure S2.1](#) in the Supplementary document to demonstrate how the pH changes over the pit surface for Cl^- concentration of $10^{-4}M$ and $10^{-3}M$. Al^{3+} , $AlCl^{2+}$, Zr^{4+} , $ZrCl^{3+}$, and $Zr(OH)Cl^{2+}$ are the main species in neutralizing the chloride ion charges in the solution. The present model assumes that 1) Al- and Zr-containing salts are sufficiently soluble during the early stages of pit growth, and 2) continuous wet environments, similar to salt fog chambers, can allow for very high concentrations of ionic species.

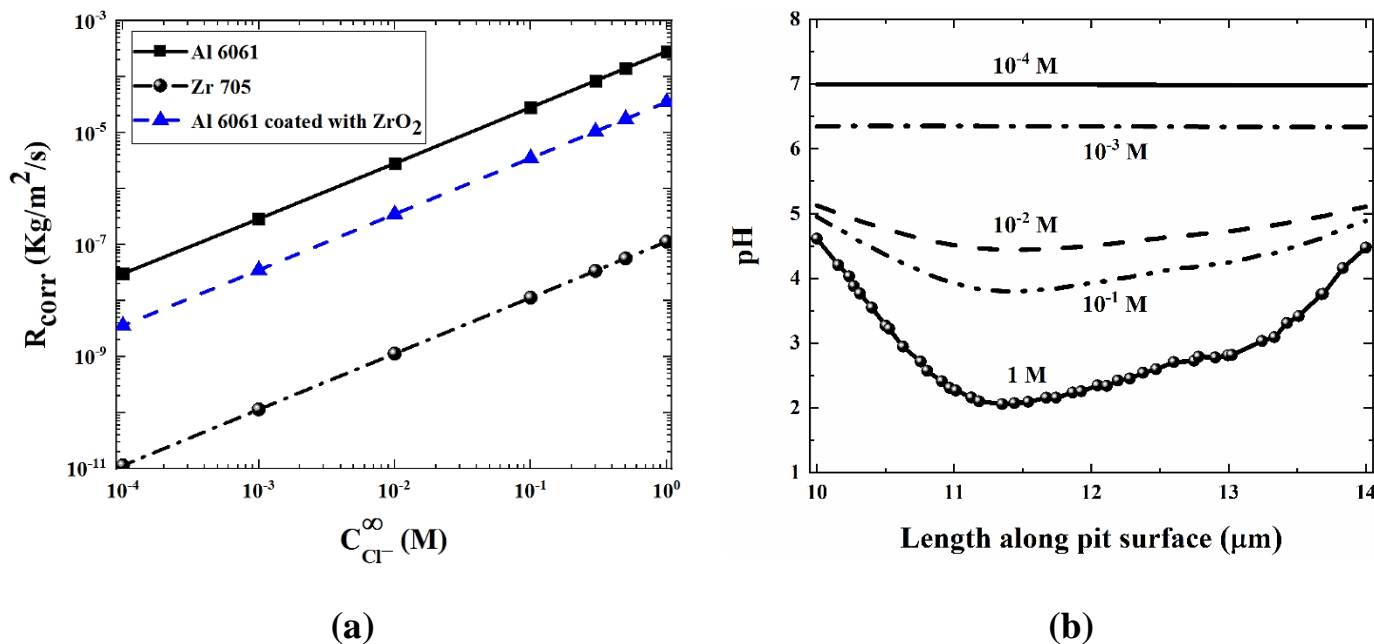


Figure 2: (a) The effect of bulk concentration of Cl^- on the corrosion rate of bare Al 6061, bare Zr 705, and Al 6061 coated with Zr-based conversion coating. It shows that the Zr-based conversion coating significantly improves the corrosion performance of aluminum alloys in NaCl solution. (b) Chemical conditions near the pit surface at a same preliminary time step showing how solution pH changes close to the pit surface for different concentrations of chloride ions. The curves for Cl^- concentrations of $10^{-4}M$ and $10^{-3}M$ are also shown in [Figure S2.1](#) in the Supplementary document to demonstrate how their pH changes over the pit surface.

[Figure 3\(a-c\)](#) depicts the anodic polarization curves obtained by using a series of constant concentrations of Cl^- and decreasing the applied potential ψ in 10 mV steps. This plot aids in determining pit stability as the repassivation potential can be quantified using the current approach. The repassivation potential, as described by Frankel et al. [91], is the potential that the pit current density falls below a critical value, which is the minimum current density required to preserve the critical pit environment and prevent repassivation. [Figure 3\(a-c\)](#) shows that the corrosion rate of the systems decreases at a fixed Cl^- concentration as the applied potential decreases from $-0.55 V$. A sharp decrease in corrosion rate indicates pit repassivation as applied potentials are reduced. The sudden growth of an aluminum oxide layer on the metal surface accurately described pit repassivation.

Furthermore, [Figure 3\(a-c\)](#) demonstrates that the repassivation potential of a system (e.g., Al 6061) decreases as the concentration of chloride ions in the solution increases. It implies that the pit surface becomes less stable when surrounded by less concentrated aggressive ions (e.g., Cl^-). Our model successfully predicted the experimentally observed behavior for aluminum alloys [88, 90]. [Figure 3\(d\)](#) compares the polarization curves of different systems (Al 6061, Zr 705, and Al 6061 with Zr-based conversion coating) at a fixed Cl^- concentration of $1M$. In comparison to the other two systems depicted in [Figure 3\(d\)](#), Al 6061 has a very high repassivation potential and a much higher corrosion rate, which is consistent with experimental observations.

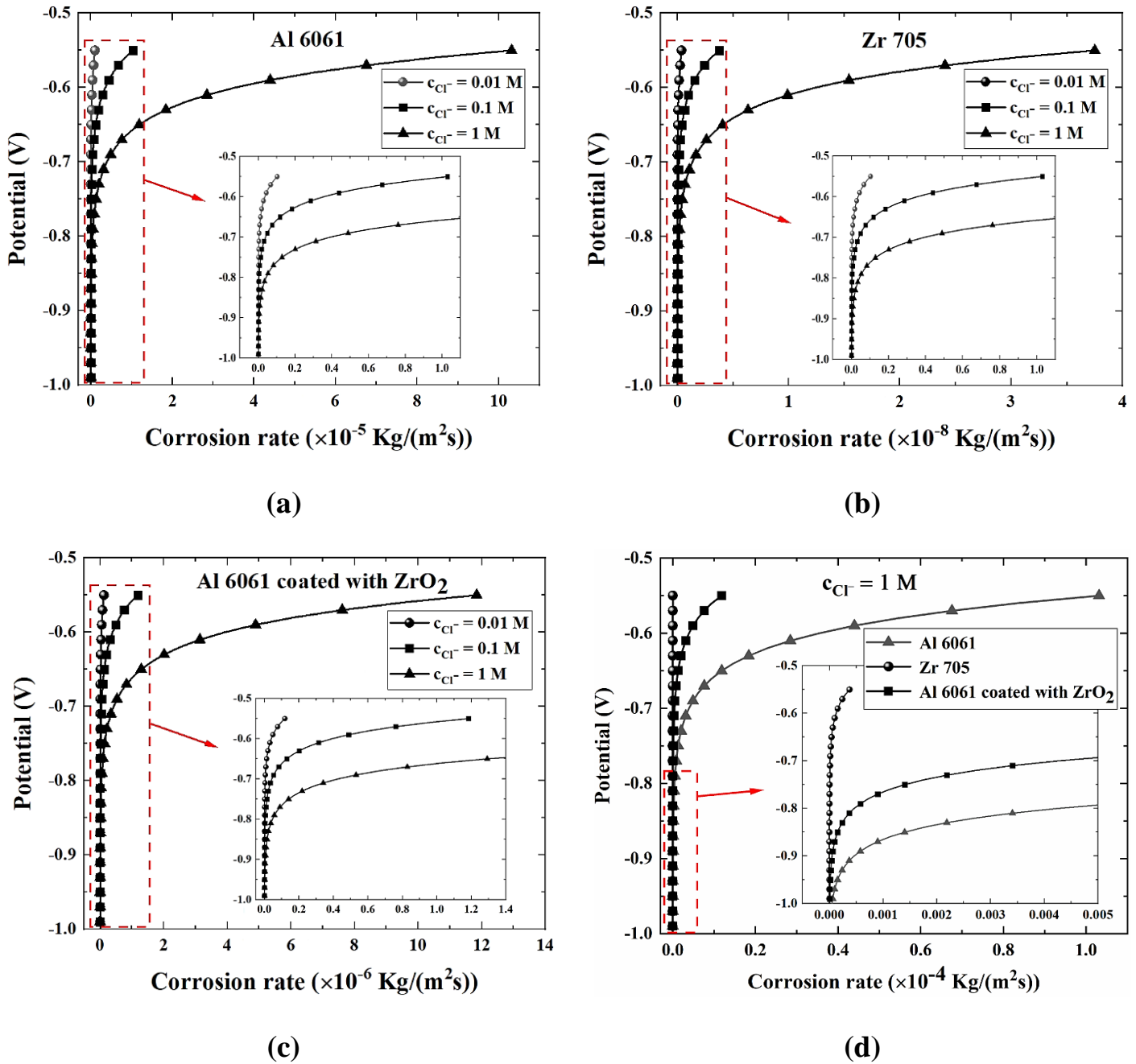


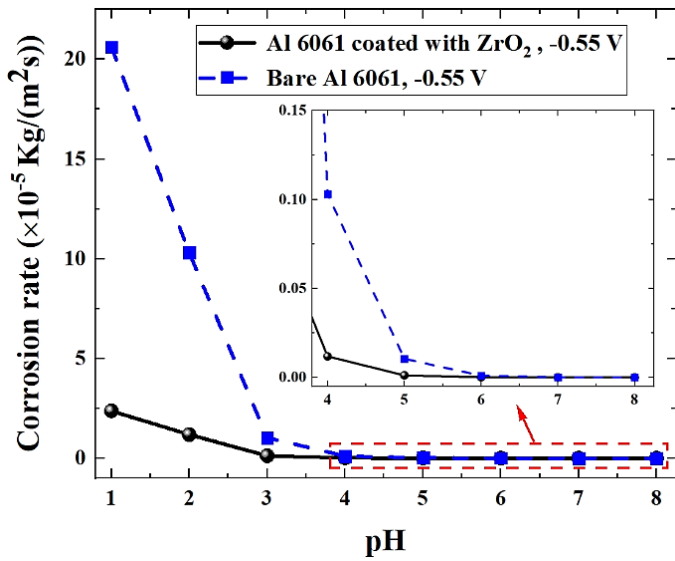
Figure 3: Anodic polarization curves for (a) bare Al 6061, (b) bare Zr 705, and (c) Al 6061 with Zr-based conversion coating at different concentrations of Cl^- . It shows that the repassivation potential decreases as the concentration of chloride ions in the solution increases. The semi-log plots for these polarization curves are shown in Figure S3.2. (d) A comparison of anodic polarization curves at $c_{Cl^-} = 1M$ for different systems.

To study the effects of pH on the corrosion rate of the systems, the concentration of chloride ions in the solution was kept constant at 0.01M. Either hydrochloric acid (HCl) or sodium hydroxide (NaOH) was used to adjust the bulk pH of the solution. Experiments have shown that when aluminum alloys are exposed to alkaline solutions, general corrosion occurs rather than localized pitting corrosion because uniform thinning of the passive oxide film (due to OH ion attack) overwhelms pitting corrosion [88]. Because localized corrosion is the focus of this research, acidic or near-neutral solutions (i.e., pH range 1 to 8) have been examined.

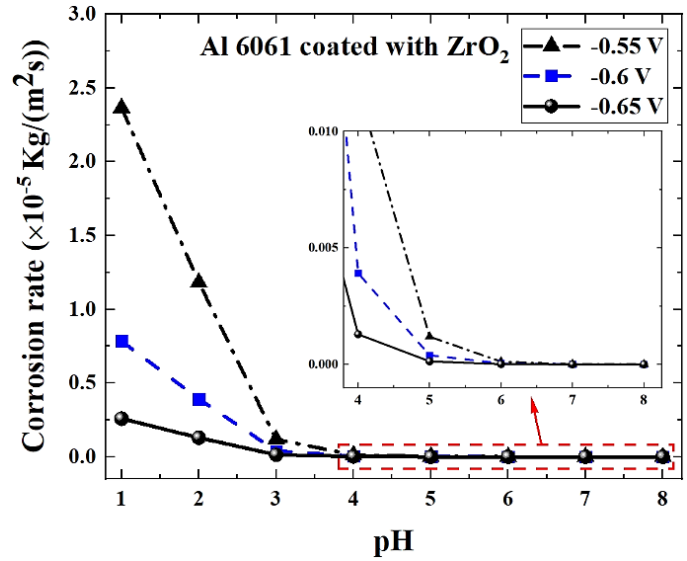
Figure 4(a) compares the corrosion rate of Al 6061 and Al 6061 with Zr-based conversion coating as a function of solution pH at a fixed applied potential of -0.55 V. The decrease in pH results in an increase in corrosion rate, which is in line with the experimental findings [92]. According to Xiao and Chaudhuri [4], there is a

critical pH above which the corrosion rate rapidly decreases to zero. Such a significant decrease shows that the pit status has changed from active to passive. The critical pH values for bare Al 6061 and Al 6061 coated with ZrO_2 are approximately 6 and 5, respectively, indicating that the presence of Zr changes the pit status in Al 6061 from active to passive at lower pH. The presence of Zr near the pit surface, on the other hand, indicates that pit stabilization is accelerated.

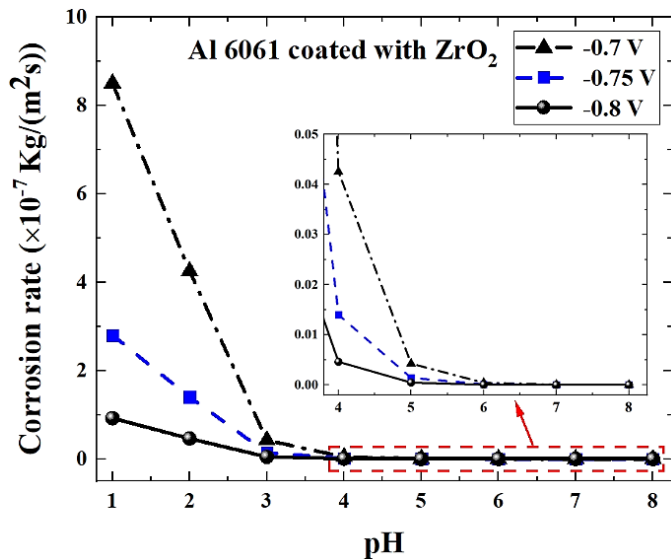
Figure 4(b) and (c) depict how the corrosion rate of Al 6061 with Zr-based conversion coating changes with pH at various applied potentials. The corrosion rate of the system increases as the solution pH decreases for different potentials due to the more acidic environment around the pit surface. At a certain pH, the corrosion rate increases as the applied potential increases. Furthermore, changes in pH between 4 and 8 have almost no effect on the corrosion rate. Figure 4(d) shows a 3D pH-potential diagram that can be used to quickly determine the corrosion rate and pit stability of Al 6061 with Zr-based conversion coating under any corrosive conditions. This 3D diagram expands on the concept of Pourbaix diagram, which shows the equilibrium phases of specific metal-electrolyte systems at various pH and potentials, by adding a new dimension of information, namely, corrosion rate. According to Figure 4(d), a more acidic environment near the pit surface results in the continuous growth of an active pit at a lower applied potential.



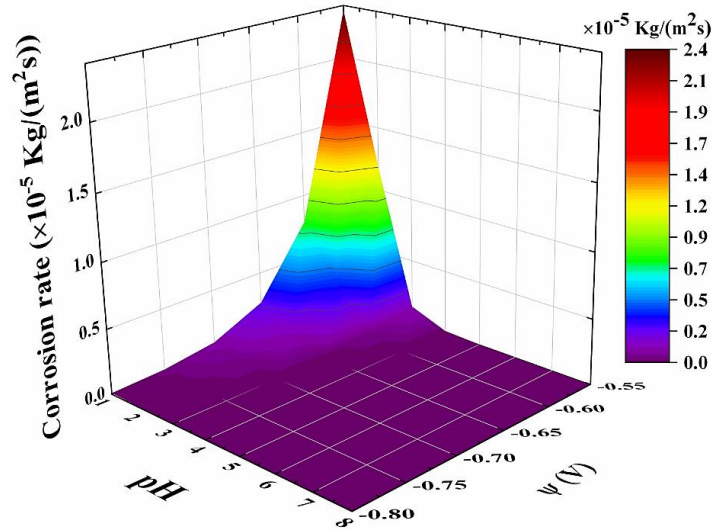
(a)



(b)



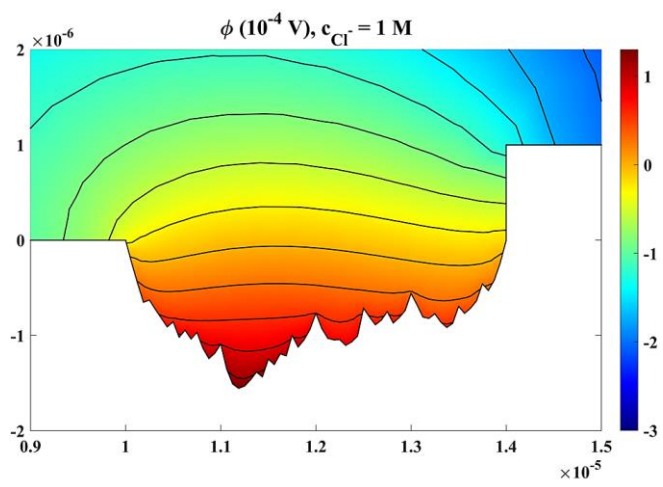
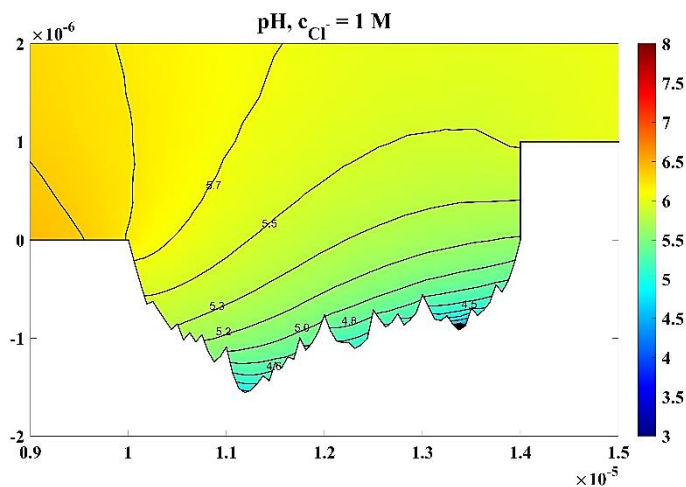
(c)



(d)

Figure 4: The effects of pH and applied potential on the performance of localized corrosion: (a) a comparison of the corrosion rates of bare Al 6061 and Al 6061 coated with ZrO_2 as a function of pH at a fixed applied potential of -0.55 V, (b) and (c) pH effects on the corrosion rate of Al 6061 coated with ZrO_2 at different applied potentials, and (d) a 3D corrosion rate-pH-applied potential diagram for Al 6061 coated with ZrO_2 . Because of the presence of Zr near the pit surface, the corrosion rate of Al 6061 coated with ZrO_2 becomes nearly zero at lower pH values compared to that of bare Al 6061.

To analyze corrosive environment within the active pit in the Al 6061 coated with ZrO_2 , Figure 5(a-f) shows 2D contour plots of pH and electrostatic potential for different concentrations of chloride ions in the system. The initial pH for these cases was set as 7, and the pH changes with increase or decrease in chloride ion concentration as it is set for each case shown in Figure 5(a, c, e). The pH contour plots indicate that the solution aggressivity increases monotonically from the pit mouth to the pit bottom. Figure 5(a, c, e) shows that as the concentration of chloride ions increases, the electrolyte within the pit becomes more acidic (i.e., has a higher H^+ concentration). This event accelerates the corrosion of systems. Figure 5(b, d, f) demonstrates that the electrostatic potentials increase from the pit mouth to the pit bottom, indicating that the ohmic potential drop in the system increases. Both ohmic potential drop and solution aggressivity affect the corrosion rate of the alloy, with the former contributing negatively and the latter positively. It should be noted that the ohmic potential effect becomes negligible as the applied potential approaches the repassivation potential [4].



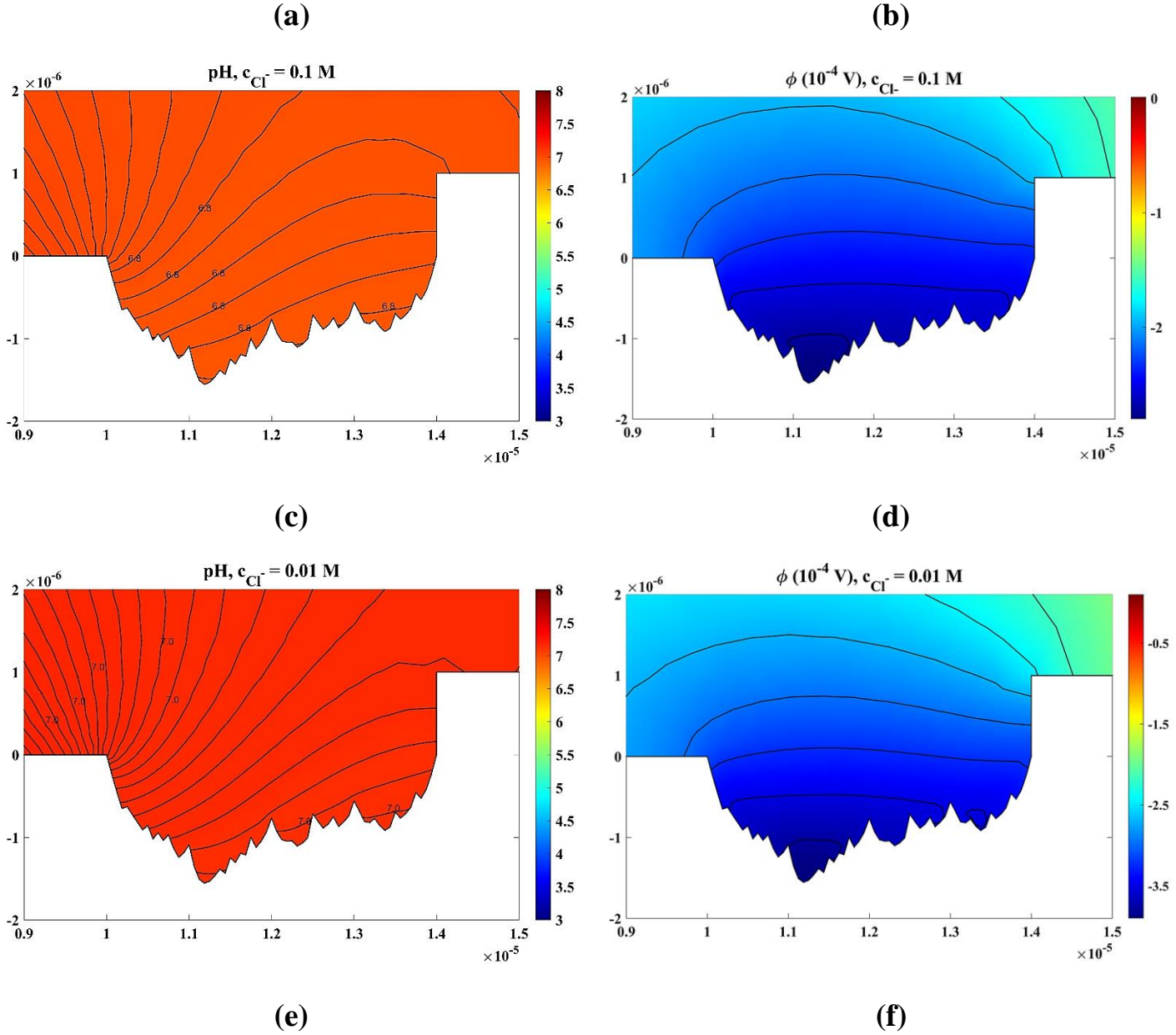


Figure 5: Corrosive environment within an active pit of Al 6061 coated with ZrO_2 : (a, c, e) 2D contour plots of solution pH at almost steady state, and (b, d, f) 2D contour plots of electrostatic potential. Plots are shown for three different concentrations of chloride ions: 0.01, 0.1, and 1 M. The unit of the pit dimension in r and z directions is meter. Figures indicate that ohmic and chemistry effects both contribute to the corrosion rate of a system, which must be taken into account as a coupled effect.

4.3 Pit Growth Dynamics

To study the dynamics of pit growth around IMPs (θ -phase), the pit depicted in Figure 1(a) is set to propagate in a neutral sodium chloride electrolyte (0.01 M) at an applied potential of -0.55 V. Figure 6 shows that the corrosion rate of both systems decreases with time throughout the corrosion process, which is consistent with experimental observations [66, 93]. The corrosion rate of Al 6061 coated with ZrO_2 approaches a near constant value during pit propagation much earlier than that of bare Al 6061. This is due to the presence of positively charged Al- and Zr-containing species in the pit that neutralize the charges and modify the local chemical environment close to the pit surface. The electrolyte solution becomes more aggressive over time (i.e., higher

concentration of chloride ions and lower pH), and the ohmic potential drop increases in the system. Thus, the net trend of the change in corrosion rate is determined by a competition between chemistry and ohmic effects.

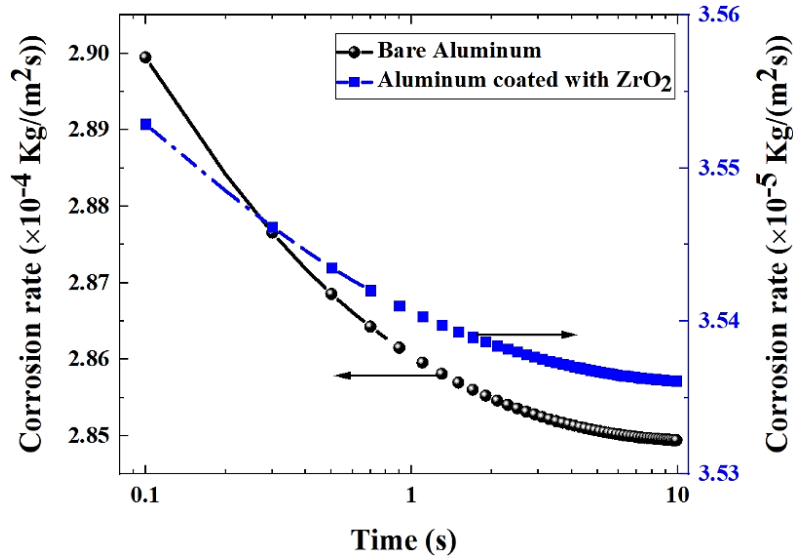
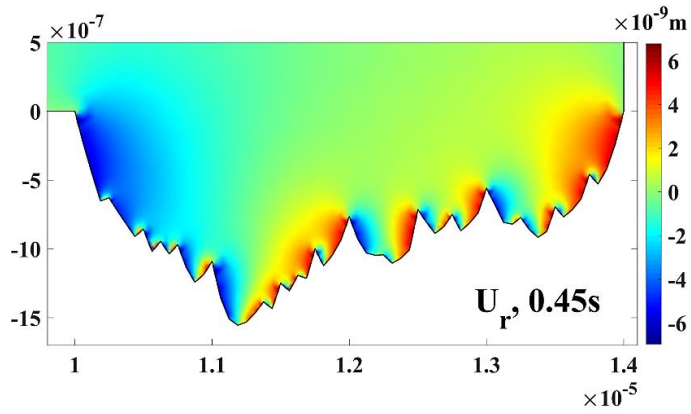


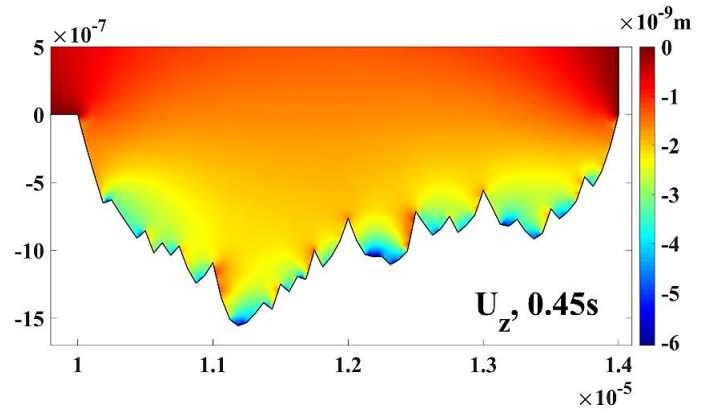
Figure 6: Dynamics of corrosion rate during pit growth for bare Al 6061 and Al 6061 with Zr-based conversion coating.

Figure 7(a-f) shows 2D contour plots of the growing pit on Al 6061 coated with ZrO_2 in the r and z – directions at different time instances. Because of the heterogeneous microstructure of aluminum alloys and moving boundary, the nature of electrochemical reactions in various locations of the pit surface was distinct and dynamically varied with time. As the pit grows in the system, more θ -phase surface is exposed. Thus, the ORR occurs on the cathodic regions (i.e., IMPs) and produces OH^- ions, which neutralizes the acidic solution in the pit, resulting in a higher pH value. Consequently, the chemistry effect (i.e., solution aggressivity) on the corrosion rate of system decreases as time proceeds. The progressively exposed Al_2O_3/ZrO_2 protection causes the pit to expand and form an occluded geometry, which contributes to a higher potential drop within the pit (can be also understood from Figure 5(b,d,f)). As a result, while the pit grows in size, the ohmic effect on corrosion of Al 6061 coated with ZrO_2 becomes more pronounced. It can be concluded that the ohmic effect outweighed the chemistry effect (which was hampered by the cathodic reaction on IMPs), resulting in an overall decrease in corrosion rate during the pit propagation. Figure 7(a-f) also presents the 2D contour plots of the growing pit on Al 6061 in r and z – directions at 0.45 seconds. At 2.494 s, this instance exhibits the same pit development as the Al 6061 coated with ZrO_2 instance, indicating that corrosion progress is much slower in Al 6061 coated with ZrO_2 than in bare Al 6061.

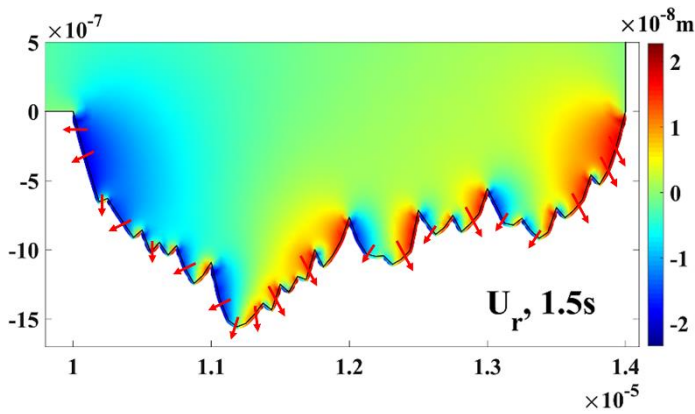
Aluminum 6061 Coated with ZrO_2



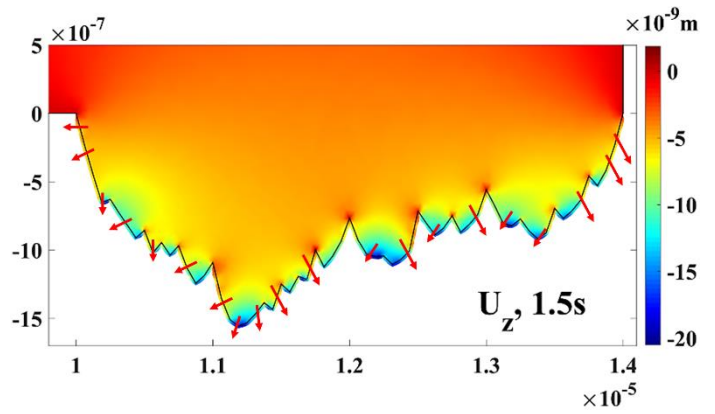
(a)



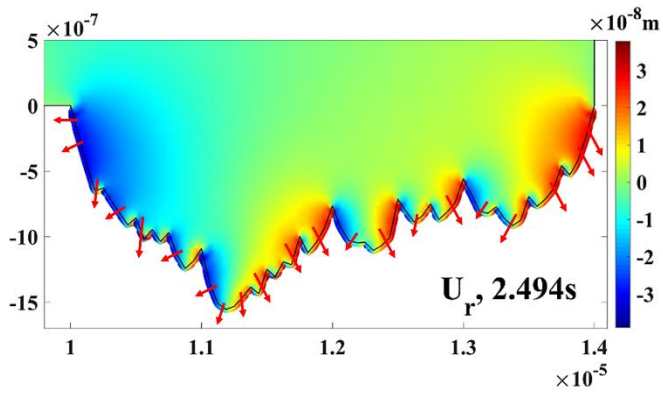
(b)



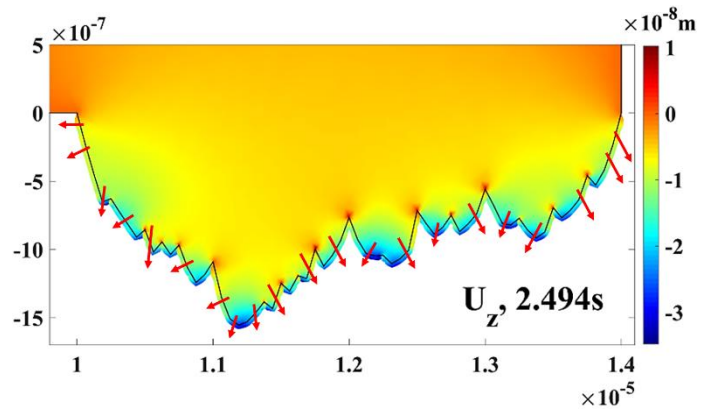
(c)



(d)



(e)



(f)

Bare Aluminum 6061

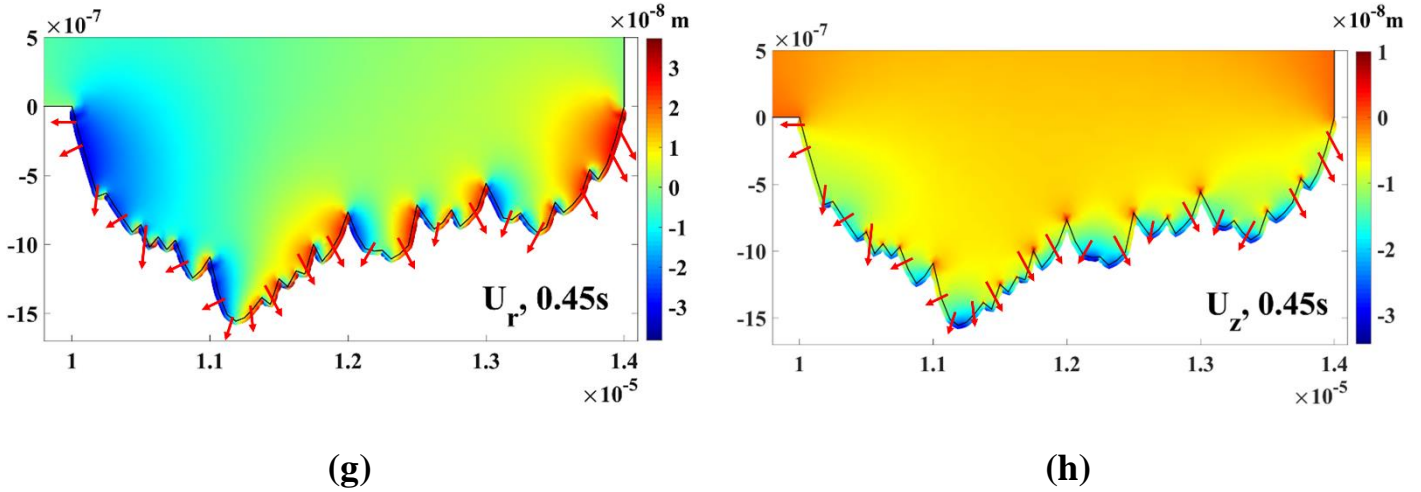


Figure 7: 2D contour plot of the growing pit in Al 6061 coated with ZrO_2 (a) U_r at 0.45 s, (b) U_z at 0.45 s, (c) U_r at 1.5 s, (d) U_z at 1.5 s, (e) U_r at 2.494 s, and (f) U_z at 2.494 s, and in bare Al 6061 (g) U_r at 0.45 s and (h) U_z at 0.45 s. U_r and U_z are the displacement in r and z directions, respectively. The unit of pit dimension in the r and z directions is meter. Comparisons show that corrosion progress in Al 6061 coated with ZrO_2 is much slower than in bare Al 6061. Arrows show the direction of pit growth during corrosion process.

5. Conclusion

A multiscale modeling framework was developed to predict the corrosion rate and pit stability of aluminum alloys with Zr-based conversion coatings. The kinetics model, which included bulk interfacial reactions, was completed using first-principles calculations and transition-state theory. By incorporating the kinetics model into multiphysics simulations, the corrosion performance of aluminum alloys with Zr-based conversion coatings was quantified for various local corrosive environments within pits, which is very difficult to establish using *in situ* experiments. The simulation results were compared to the results of experiments reported in the literature, and they showed excellent agreements for corrosion rates of different alloys. Furthermore, good agreement was found between the DFT-TST results and experimental data for the rate constants of bulk first-order reactions occurring in the electrolyte. Later, the model was employed to quantitatively explore the effects of local corrosive environments on the corrosion performance of aluminum alloys coated with ZrO_2 . The local corrosive fields (i.e., chemical and electrical conditions) were determined within the localized pits at different solution conditions. The following are some of the key findings from simulation results for certain electrochemical conditions as elucidated in this work: 1) a Zr-based conversion coating significantly improves the corrosion performance of aluminum alloys due to the presence of zirconium in interfacial kinetics, 2) the repassivation potential of a system (e.g., Al 6061) decreases as the concentration of chloride ions in the solution increases, leading to a less stable pit, and 3) the critical pH value for Al 6061 coated with ZrO_2 is lower than for bare Al 6061 because the presence of Zr changes the pit status from active to passive at lower pH.

Data Availability

All the required data that support the findings of this study are available in the paper.

Acknowledgments

This work was supported by the Strategic Environmental Research and Development Program (SERDP) under project WP-2742. We would like to thank the experimental team at the Center for Plasma Materials Interactions

(CPMPI) of the University of Illinois at Urbana-Champaign for their sustained effort in developing these coatings using atmospheric pressure plasma and providing us with corrosion data of the components.

Reference

- [1] A. Boag, R. Taylor, T. Muster, N. Goodman, D. McCulloch, C. Ryan, B. Rout, D. Jamieson, A. Hughes, Stable pit formation on AA2024-T3 in a NaCl environment, *Corrosion Sci.* 52(1) (2010) 90-103.
- [2] A. Hughes, A. Boag, A. Glenn, D. McCulloch, T. Muster, C. Ryan, C. Luo, X. Zhou, G. Thompson, Corrosion of AA2024-T3 Part II: Co-operative corrosion, *Corrosion Sci.* 53(1) (2011) 27-39.
- [3] O. Guseva, P. Schmutz, T. Suter, O. von Trzebiatowski, Modelling of anodic dissolution of pure aluminium in sodium chloride, *Electrochim. Acta* 54(19) (2009) 4514-4524.
- [4] J. Xiao, S. Chaudhuri, Predictive modeling of localized corrosion: an application to aluminum alloys, *Electrochim. Acta* 56(16) (2011) 5630-5641.
- [5] A. Boag, A. Hughes, N. Wilson, A. Torpy, C. MacRae, A. Glenn, T. Muster, How complex is the microstructure of AA2024-T3?, *Corrosion Sci.* 51(8) (2009) 1565-1568.
- [6] Y. Zhu, K. Sun, J. Garves, L.G. Bland, J. Locke, J. Allison, G. Frankel, Micro-and nano-scale intermetallic phases in AA2070-T8 and their corrosion behavior, *Electrochim. Acta* 319 (2019) 634-648.
- [7] A. Kosari, F. Tichelaar, P. Visser, H. Zandbergen, H. Terryn, J. Mol, Dealloying-driven local corrosion by intermetallic constituent particles and dispersoids in aerospace aluminium alloys, *Corrosion Sci.* 177 (2020) 108947.
- [8] R. Buchheit, R. Grant, P. Hlava, B. McKenzie, G. Zender, Local dissolution phenomena associated with S phase (Al₂CuMg) particles in aluminum alloy 2024-T3, *Journal of the electrochemical society* 144(8) (1997) 2621.
- [9] Y. Yoon, R. Buchheit, Dissolution behavior of Al₂CuMg (S phase) in chloride and chromate conversion coating solutions, *Journal of The Electrochemical Society* 153(5) (2006) B151.
- [10] N. Birbilis, R. Buchheit, Investigation and discussion of characteristics for intermetallic phases common to aluminum alloys as a function of solution pH, *Journal of the Electrochemical Society* 155(3) (2008) C117.
- [11] K.D. Ralston, T.L. Young, R.G. Buchheit, Electrochemical evaluation of constituent intermetallics in aluminum alloy 2024-T3 exposed to aqueous vanadate inhibitors, *Journal of the electrochemical society* 156(4) (2009) C135.
- [12] R. Grilli, M.A. Baker, J.E. Castle, B. Dunn, J.F. Watts, Localized corrosion of a 2219 aluminium alloy exposed to a 3.5% NaCl solution, *Corrosion Sci.* 52(9) (2010) 2855-2866.
- [13] S.-I. Pyun, E.-J. Lee, Effect of halide ion and applied potential on repassivation behaviour of Al-1 wt.% Si-0.5 wt.% Cu alloy, *Electrochim. Acta* 40(12) (1995) 1963-1970.
- [14] G. Williams, A.J. Coleman, H.N. McMurray, Inhibition of Aluminium Alloy AA2024-T3 pitting corrosion by copper complexing compounds, *Electrochim. Acta* 55(20) (2010) 5947-5958.
- [15] J. Li, N. Birbilis, R.G. Buchheit, Electrochemical assessment of interfacial characteristics of intermetallic phases present in aluminium alloy 2024-T3, *Corrosion Sci.* 101 (2015) 155-164.

- [16] Y. Zhu, K. Sun, G. Frankel, Intermetallic phases in aluminum alloys and their roles in localized corrosion, *Journal of The Electrochemical Society* 165(11) (2018) C807.
- [17] R. Oltra, B. Malki, F. Rechou, Influence of aeration on the localized trenching on aluminium alloys, *Electrochim. Acta* 55(15) (2010) 4536-4542.
- [18] A.S.H. Makhlof, *Handbook of smart coatings for materials protection*, Elsevier 2014.
- [19] I. Milošev, G. Frankel, conversion coatings based on zirconium and/or Titanium, *Journal of The Electrochemical Society* 165(3) (2018) C127.
- [20] J. Zhao, G. Frankel, R.L. McCreery, Corrosion protection of untreated AA-2024-T3 in chloride solution by a chromate conversion coating monitored with Raman spectroscopy, *Journal of the Electrochemical Society* 145(7) (1998) 2258.
- [21] H.J. Gibb, P.S. Lees, P.F. Pinsky, B.C. Rooney, Lung cancer among workers in chromium chemical production, *American journal of industrial medicine* 38(2) (2000) 115-126.
- [22] P.L. Bidstrup, R. Case, Carcinoma of the lung in workmen in the chromates-producing industry in Great Britain, *British journal of industrial medicine* 13(4) (1956) 260.
- [23] J. Nordlien, J. Walmsley, H. Østerberg, K. Nisancioglu, Formation of a zirconium-titanium based conversion layer on AA 6060 aluminium, *Surface and Coatings Technology* 153(1) (2002) 72-78.
- [24] F. George, P. Skeldon, G. Thompson, Formation of zirconium-based conversion coatings on aluminium and Al-Cu alloys, *Corrosion Sci.* 65 (2012) 231-237.
- [25] X. Zhong, X. Wu, Y. Jia, Y. Liu, Self-repairing vanadium-zirconium composite conversion coating for aluminum alloys, *Appl. Surf. Sci.* 280 (2013) 489-493.
- [26] S.S. Golru, M. Attar, B. Ramezanzadeh, Morphological analysis and corrosion performance of zirconium based conversion coating on the aluminum alloy 1050, *J. Ind. Eng. Chem.* 24 (2015) 233-244.
- [27] J. Gray, B. Luan, Protective coatings on magnesium and its alloys—a critical review, *Journal of alloys and compounds* 336(1-2) (2002) 88-113.
- [28] P. Zhou, Y. Liu, L. Liu, B. Yu, T. Zhang, F. Wang, Critical role of pretreatment on the corrosion resistance of Zr conversion coating on 6061 aluminum alloy: The combined effect of surface topography and potential difference between different phases, *Surface and Coatings Technology* 377 (2019) 124904.
- [29] J. Han, D. Thierry, K. Ogle, Zr-based conversion coating on Zn and Zn-Al-Mg alloy coating: Understanding the accelerating effect of Cu (II) and NO₃⁻, *Surface and Coatings Technology* 402 (2020) 126236.
- [30] J. Cerezo, I. Vandendael, R. Posner, K. Lill, J. De Wit, J. Mol, H. Terryn, Initiation and growth of modified Zr-based conversion coatings on multi-metal surfaces, *Surface and Coatings Technology* 236 (2013) 284-289.
- [31] J. Cerezo, P. Taheri, I. Vandendael, R. Posner, K. Lill, J.H.W. de Wit, J. Mol, H. Terryn, Influence of surface hydroxyls on the formation of Zr-based conversion coatings on AA6014 aluminum alloy, *Surface and coatings technology* 254 (2014) 277-283.
- [32] X. Liu, D. Vonk, H. Jiang, K. Kisslinger, X. Tong, M. Ge, E. Nazaretski, B. Ravel, K. Foster, S. Petrash, Environmentally friendly Zr-based conversion nanocoatings for corrosion inhibition of metal surfaces evaluated by multimodal x-ray analysis, *ACS Applied Nano Materials* 2(4) (2019) 1920-1929.

- [33] T. Lostak, A. Maljusch, B. Klink, S. Krebs, M. Kimpel, J. Flock, S. Schulz, W. Schuhmann, Zr-based conversion layer on Zn-Al-Mg alloy coated steel sheets: insights into the formation mechanism, *Electrochim. Acta* 137 (2014) 65-74.
- [34] J. Cerezo, I. Vandendael, R. Posner, J. De Wit, J. Mol, H. Terryn, The effect of surface pre-conditioning treatments on the local composition of Zr-based conversion coatings formed on aluminium alloys, *Appl. Surf. Sci.* 366 (2016) 339-347.
- [35] S. Sharland, A review of the theoretical modelling of crevice and pitting corrosion, *Corrosion Sci.* 27(3) (1987) 289-323.
- [36] M. Verhoff, R. Alkire, Experimental and modeling studies of single pits on pure aluminum in ph 11 nacl solutions i. Laser initiated single pits, *Journal of the Electrochemical Society* 147(4) (2000) 1349.
- [37] N. Murer, R. Oltra, B. Vuillemin, O. Néel, Numerical modelling of the galvanic coupling in aluminium alloys: A discussion on the application of local probe techniques, *Corrosion Sci.* 52(1) (2010) 130-139.
- [38] K.B. Deshpande, Validated numerical modelling of galvanic corrosion for couples: Magnesium alloy (AE44)–mild steel and AE44–aluminium alloy (AA6063) in brine solution, *Corrosion Sci.* 52(10) (2010) 3514-3522.
- [39] L. Abodi, J. DeRose, S. Van Damme, A. Demeter, T. Suter, J. Deconinck, Modeling localized aluminum alloy corrosion in chloride solutions under non-equilibrium conditions: steps toward understanding pitting initiation, *Electrochim. Acta* 63 (2012) 169-178.
- [40] L. Yin, Y. Jin, C. Leygraf, J. Pan, A FEM model for investigation of micro-galvanic corrosion of Al alloys and effects of deposition of corrosion products, *Electrochim. Acta* 192 (2016) 310-318.
- [41] O. Guseva, J. DeRose, P. Schmutz, Modelling the early stage time dependence of localised corrosion in aluminium alloys, *Electrochim. Acta* 88 (2013) 821-831.
- [42] W. Mai, S. Soghrati, New phase field model for simulating galvanic and pitting corrosion processes, *Electrochim. Acta* 260 (2018) 290-304.
- [43] W. Mai, S. Soghrati, R.G. Buchheit, A phase field model for simulating the pitting corrosion, *Corrosion Sci.* 110 (2016) 157-166.
- [44] L. Yin, Y. Jin, C. Leygraf, N. Birbilis, J. Pan, Numerical simulation of micro-galvanic corrosion in Al alloys: effect of geometric factors, *Journal of The Electrochemical Society* 164(2) (2017) C75.
- [45] S.R. Cross, S. Gollapudi, C.A. Schuh, Validated numerical modeling of galvanic corrosion of zinc and aluminum coatings, *Corrosion Sci.* 88 (2014) 226-233.
- [46] L. Yin, Y. Jin, C. Leygraf, J. Pan, Numerical simulation of micro-galvanic corrosion of Al alloys: Effect of chemical factors, *Journal of The Electrochemical Society* 164(13) (2017) C768.
- [47] A. Sumer, S. Chaudhuri, A first principles investigation of corrosion chemistry of common elemental impurities in Mg-Al alloys, *Corrosion* 73(5) (2017) 596-604.
- [48] S.R. Cross, C.A. Schuh, Modeling localized corrosion with an effective medium approximation, *Corrosion Sci.* 116 (2017) 53-65.

- [49] N. Li, C. Dong, C. Man, X. Li, D. Kong, Y. Ji, M. Ao, J. Cao, L. Yue, X. Liu, Insight into the localized strain effect on micro-galvanic corrosion behavior in AA7075-T6 aluminum alloy, *Corrosion Sci.* 180 (2021) 109174.
- [50] Y. Zhu, J.D. Poplawsky, S. Li, R.R. Unocic, L.G. Bland, C.D. Taylor, J.S. Locke, E.A. Marquis, G.S. Frankel, Localized corrosion at nm-scale hardening precipitates in Al-Cu-Li alloys, *Acta Materialia* 189 (2020) 204-213.
- [51] L. Bailly-Salins, L. Borrel, W. Jiang, B.W. Spencer, K. Shirvan, A. Couet, Modeling of High-Temperature Corrosion of Zirconium Alloys Using the eXtended Finite Element Method (X-FEM), *Corrosion Sci.* (2021) 109603.
- [52] S.K. Sankaranarayanan, S. Ramanathan, Molecular dynamics simulation study of nanoscale passive oxide growth on Ni-Al alloy surfaces at low temperatures, *Physical review b* 78(8) (2008) 085420.
- [53] B. Diawara, M. Legrand, J.-J. Legendre, P. Marcus, Use of quantum chemistry results in 3D modeling of corrosion of iron-chromium alloys, *Journal of the Electrochemical Society* 151(3) (2004) B172.
- [54] D. Gunasegaram, M. Venkatraman, I. Cole, Towards multiscale modelling of localised corrosion, *Int. Mater. Rev.* 59(2) (2014) 84-114.
- [55] J. Xiao, H. Kwak, T. Chastek, S. Chaudhuri, Simulations Guided Design of Anti-Corrosion Coatings for Al Alloys by Selective Targeting of Intermetallic Particles, *Proceedings of Materials Science and Technology (MS&T)*, Columbus, OH, 2011, pp. 1173-1182.
- [56] S. Dong, W. Shi, J. Zhang, S. Bi, DFT studies on the water-assisted synergistic proton dissociation mechanism for the spontaneous hydrolysis reaction of Al^{3+} in aqueous solution, *ACS Earth and Space Chemistry* 2(3) (2018) 269-277.
- [57] P. Giannozzi, S. Baroni, N. Bonini, M. Calandra, R. Car, C. Cavazzoni, D. Ceresoli, G.L. Chiarotti, M. Cococcioni, I. Dabo, QUANTUM ESPRESSO: a modular and open-source software project for quantum simulations of materials, *Journal of physics: Condensed matter* 21(39) (2009) 395502.
- [58] J.P. Perdew, K. Burke, M. Ernzerhof, Generalized gradient approximation made simple, *Phys. Rev. Lett.* 77(18) (1996) 3865.
- [59] G. Henkelman, H. Jónsson, Improved tangent estimate in the nudged elastic band method for finding minimum energy paths and saddle points, *The Journal of chemical physics* 113(22) (2000) 9978-9985.
- [60] G. Henkelman, B.P. Uberuaga, H. Jónsson, A climbing image nudged elastic band method for finding saddle points and minimum energy paths, *The Journal of chemical physics* 113(22) (2000) 9901-9904.
- [61] S. Kundu, S. Bhattacharjee, S.-C. Lee, M. Jain, PASTA: Python Algorithms for Searching Transition states, *Comput. Phys. Commun.* 233 (2018) 261-268.
- [62] F.P. Rotzinger, The Water-Exchange Mechanism of the $[UO_2(OH)_2]^{2+}$ Ion Revisited: The Importance of a Proper Treatment of Electron Correlation, *Chemistry—A European Journal* 13(3) (2007) 800-811.
- [63] D. Macdonald, G. Engelhardt, Predictive modeling of corrosion, *Shreir's Corros*, Elsevier BV 2 (2010) 1630-1679.
- [64] A. Anderko, N. Sridhar, D. Dunn, A general model for the repassivation potential as a function of multiple aqueous solution species, *Corrosion Sci.* 46(7) (2004) 1583-1612.

- [65] G. Engelhardt, D.D. Macdonald, Unification of the deterministic and statistical approaches for predicting localized corrosion damage. I. Theoretical foundation, *Corrosion Sci.* 46(11) (2004) 2755-2780.
- [66] K.P. Wong, R.C. Alkire, Local chemistry and growth of single corrosion pits in aluminum, *Journal of the Electrochemical Society* 137(10) (1990) 3010.
- [67] H. Groult, A. Barhoun, H. El Ghallali, S. Borensztjan, F. Lantelme, Study of the electrochemical reduction of Zr⁴⁺ ions in molten alkali fluorides, *Journal of the electrochemical society* 155(2) (2007) E19.
- [68] M. Sosna, G. Denuault, R.W. Pascal, R.D. Prien, M. Mowlem, Development of a reliable microelectrode dissolved oxygen sensor, *Sensors and Actuators B: Chemical* 123(1) (2007) 344-351.
- [69] T.H. Osterheld, M.D. Allendorf, C.F. Melius, Unimolecular decomposition of methyltrichlorosilane: RRKM calculations, *The Journal of Physical Chemistry* 98(28) (1994) 6995-7003.
- [70] Y. Liu, Y. Yang, C. Zhang, T. Zhang, B. Yu, G. Meng, Y. Shao, F. Wang, L. Liu, Protection of AA5083 by a zirconium-based conversion coating, *Journal of The Electrochemical Society* 163(9) (2016) C576.
- [71] G. Šekularac, J. Kovač, I. Milošev, Prolonged protection, by zirconium conversion coatings, of AlSi7Mg0.3 aluminium alloy in chloride solution, *Corrosion Sci.* 169 (2020) 108615.
- [72] Y.-S. Kim, J.G. Park, B.-S. An, Y.H. Lee, C.-W. Yang, J.-G. Kim, Investigation of zirconium effect on the corrosion resistance of aluminum alloy using electrochemical methods and numerical simulation in an acidified synthetic sea salt solution, *Materials* 11(10) (2018) 1982.
- [73] C. Baes, R. Mesmer, *The Hydrolysis of Cations*, John Wiley and Sons, New York, NY, 1976.
- [74] E. Curti, C. Degueldre, Solubility and hydrolysis of Zr oxides: a review and supplemental data, *Radiochim. Acta* 90(9-11) (2002) 801-804.
- [75] M. Pourbaix, *Atlas of electrochemical equilibria in aqueous solution*, NACE 307 (1974).
- [76] L.P. Holmes, D.L. Cole, E.M. Eyring, Kinetics of aluminum ion hydrolysis in dilute solutions, *The Journal of Physical Chemistry* 72(1) (1968) 301-304.
- [77] T.L. Brown, H.E. LeMay Jr, B.E. Bursten, *Chemical thermodynamics, Chemical Thermodynamics of Zirconium*. NEA OECD, Elsevier, ISBN-13 (2005) 978-0.
- [78] T. Nguyen, R. Foley, The chemical nature of aluminum corrosion: II. The initial dissolution step, *Journal of the Electrochemical Society* 129(1) (1982) 27.
- [79] R. Turner, G. Ross, Conditions in solution during the formation of gibbsite in dilute Al salt solutions. 4. Effect of Cl concentration and temperature and a proposed mechanism for gibbsite formation, *Canadian Journal of Chemistry* 48(5) (1970) 723-729.
- [80] M. Eigen, L. De Maeyer, Untersuchungen über die Kinetik der Neutralisation. I, *Zeitschrift für Elektrochemie, Berichte der Bunsengesellschaft für physikalische Chemie* 59(10) (1955) 986-993.
- [81] M. Starostin, G. Shter, G. Grader, Corrosion of aluminum alloys Al 6061 and Al 2024 in ammonium nitrate-urea solution, *Materials and Corrosion* 67(4) (2016) 387-395.
- [82] W. Ferrando, *Zirconium as a structural material for naval systems*, Naval surface weapons center silver spring MD, 1985.

- [83] T. Yau, R. Webster, Corrosion of zirconium and hafnium, Metals handbook ninth edition. Volume 13. Corrosion 1987.
- [84] This data are provided by our experimental collaborator in the Center for Plasma Materials Interactions (CPMPI) under Professor David N Ruzic at the University of Illinois at Urbana-Champaign, which will be published in the near future. .
- [85] B. Zaid, D. Saidi, A. Benzaid, S. Hadji, Effects of pH and chloride concentration on pitting corrosion of AA6061 aluminum alloy, Corrosion Sci. 50(7) (2008) 1841-1847.
- [86] Y. Guo, G.S. Frankel, Characterization of trivalent chromium process coating on AA2024-T3, Surface and Coatings Technology 206(19-20) (2012) 3895-3902.
- [87] S. Pride, J. Scully, J. Hudson, Metastable pitting of aluminum and criteria for the transition to stable pit growth, Journal of the Electrochemical Society 141(11) (1994) 3028.
- [88] G. Frankel, J. Scully, C. Jahnes, Repassivation of pits in aluminum thin films, Journal of the Electrochemical Society 143(6) (1996) 1834.
- [89] V. Branzoi, F. Golgovici, F. Branzoi, Aluminium corrosion in hydrochloric acid solutions and the effect of some organic inhibitors, Mater. Chem. Phys. 78(1) (2003) 122-131.
- [90] D.W. Buzza, R.C. Alkire, Growth of corrosion pits on pure aluminum in 1M NaCl, Journal of the Electrochemical Society 142(4) (1995) 1104.